Journal of Controlled Release 390 (2026) 114562

Contents lists available at ScienceDirect

Journal of Controlled Release

journal homepage: www.elsevier.com/locate/jconrel

# Octopus-inspired polymeric nanovaccine enables high antigen loading and robust T cell activation for cancer immunotherapy

Zijuan Wang [a,e,1], Yuanzhen Su [a,b,1], Shucheng Zhang [a], Bingzheng Yu [a], Dongbo Chen [c], Xiang Gao [d], Yan Wei [e], Irina A. Veselova [f], Mingqiang Li [g], Shixian Lv [a,*]

[a] Key Laboratory of Polymer Chemistry and Physics of Ministry of Education, School of Materials Science and Engineering, Peking University, Beijing 100871, China
[b] Key Laboratory of Polymer Ecomaterials, Changchun Institute of Applied Chemistry, Chinese Academy of Sciences, Changchun 130022, China
[c] Infectious Disease and Hepatology Center of Peking University People's Hospital, Peking University Hepatology Institute, Peking University People's Hospital, Beijing 100044, China
[d] Department of Gastrointestinal Surgery, West China School of Medicine, Institute of Digestive Surgery, West China Hospital, Sichuan University, Chengdu 610041, China
[e] Department of Geriatric Dentistry, NMPA Key Laboratory for Dental Materials, National Engineering Laboratory for Digital and Material Technology of Stomatology, Peking University School and Hospital of Stomatology, Beijing 100081, China
[f] Department of Chemistry, Lomonosov Moscow State University, Moscow 119991, Russia
[g] Laboratory of Biomaterials and Translational Medicine, Center for Nanomedicine and Department of Ultrasound, The Third Affiliated Hospital, Sun Yat-sen University, Guangzhou 510630, China

ARTICLE INFO

*Keywords:*
Cancer vaccine
Polymer adjuvant
Nano-octopus
Polymer carriers
Cancer immunotherapy

ABSTRACT

Tumor vaccines hold significant promise for immunotherapy, but are limited by low antigen loading capacity, inefficient cytosolic delivery, and suboptimal T cell activation. Here, we present an octopus-inspired polymeric nanovaccine that integrates high antigen-loading capacity and effective cytosolic delivery within a single polymeric platform. The nanovaccine is constructed by encapsulating antigens with an imidazole-functionalized fluorinated polyethyleneimine and $Mn^{2+}$ ions, forming a structure that mimics octopus tentacles and suction cups, where the PEI backbone acts as tentacle-like arms and the imidazole-$Mn^{2+}$ units serve as suction cups. This multivalent interface enables robust antigen binding through electrostatic, coordination, and hydrophobic interactions. Beyond stabilizing the antigen payload, the amphiphilic cationic design of the polymers offers efficient cytosolic delivery of antigens into dendritic cells (DCs). Meanwhile, the intracellular release of $Mn^{2+}$ activates the STING pathway, promoting innate immune responses. Consequently, the vaccine elicits robust antigen-specific $CD8^+$ T cell responses and durable antitumor immunity in multiple tumor models. This work presents a streamlined, multifunctional strategy to overcome delivery barriers in cancer vaccines.

## 1. Introduction

Therapeutic vaccines represent a promising strategy for cancer immunotherapy and have garnered considerable attention [1–4]. Despite the advancement of several candidates into clinical trials, their overall efficacy remains limited, primarily due to poor antigen delivery and inefficient cytosolic transport in dendritic cells (DCs), which result in suboptimal cross-presentation and low immunogenicity [5–8]. Under physiological conditions, vaccine antigens need to be drained to lymph nodes (LNs) and effectively captured by local antigen-presenting cells (APCs) [9–11]. However, soluble protein antigens exhibit poor uptake by APCs and are often degraded within lysosomes following endocytosis, thereby hindering cytosolic delivery and impairing antigen cross-presentation [12–14]. Therefore, the development of vaccine carriers capable of efficient delivery of tumor antigens to DCs has become a key breakthrough in tumor vaccine research and development.

The rapid development of nanotechnology has opened new avenues for vaccine design [15–18]. Among these, polymeric nanovaccines have garnered significant interest due to their tunable architectures and multifunctionality [19–21]. For instance, poly(lactic-*co*-glycolic acid) (PLGA) nanoparticles can encapsulate antigens to protect them from enzymatic degradation and prolong immune stimulation [22–24]. The

* Corresponding author.
*E-mail address:* lvshixian@pku.edu.cn (S. Lv).
[1] These authors contributed equally to this work.

https://doi.org/10.1016/j.jconrel.2025.114562
Received 20 November 2025; Received in revised form 17 December 2025; Accepted 19 December 2025
Available online 20 December 2025

ultra-pH-sensitive poly(cyclodextrin-7-amine) (PC7A) has been reported to promote type I interferon responses in DCs, through modulation of the stimulator of interferon genes (STING) pathway [25,26]. Furthermore, polyethyleneimines (PEI) modified with hydrophobic moieties have demonstrated improved DC maturation through innate immune activation [27,28]. Recent advances have also explored viromimetic polymeric vaccines, which mimic virus-like structures to enhance immune response and improve cancer vaccine efficacy [29,30]. Nevertheless, most tumor antigens, including peptides and proteins, possess complex structures, are prone to enzymatic degradation, and exhibit low loading efficiencies, posing significant challenges for delivery systems in overcoming biological barriers and achieving effective anti-tumor immune responses [31,32]. Although polymer carriers show great promise for vaccine delivery, integrating multiple immunological functions into a single platform remains challenging. Therefore, designing nanocarriers capable of high antigen loading, efficient cytosolic delivery and coordinated immune stimulation remains challenging for cancer vaccine.

Octopuses capture prey through their soft, flexible tentacles and the numerous suckers. Inspired by the octopus's multivalent prey-capture mechanism utilizing tentacles and adhesive suckers, we developed a polymeric nanovaccine platform integrating high antigen-loading capacity, efficient cytosolic delivery, and self-adjuvant properties (Scheme 1). The nano-octopus vaccine was constructed by *co*-assembling the antigen with imidazole-functionalized fluorinated polyethyleneimine (PEI-F-M) and $Mn^{2+}$. This design draws inspiration from the multivalent capture strategy of octopus tentacles: the PEI backbone serves as tentacle-like arms, while midazole-$Mn^{2+}$ units mimic suction cups, enabling stable antigen capture via electrostatic, coordination, and hydrophobic interactions. After subcutaneous injection, the nanovaccine efficiently accumulates in draining lymph nodes (DLNs) and is actively internalized by DCs, promoting cytosolic delivery of antigens and enhancing DCs maturation and antigen cross-presentation. Concurrently, the intracellular release of $Mn^{2+}$ activates the STING pathway, driving robust immune activation. Functionally, the nano-octopus vaccine induces strong antigen-specific $CD8^+$ T cell responses and promotes potent antitumor effects. In summary, this multifunctional polymeric nanovaccine integrates STING activation, biomimetic antigen capture, and imidazole-mediated endosomal escape, offering a promising approach for cancer vaccination.

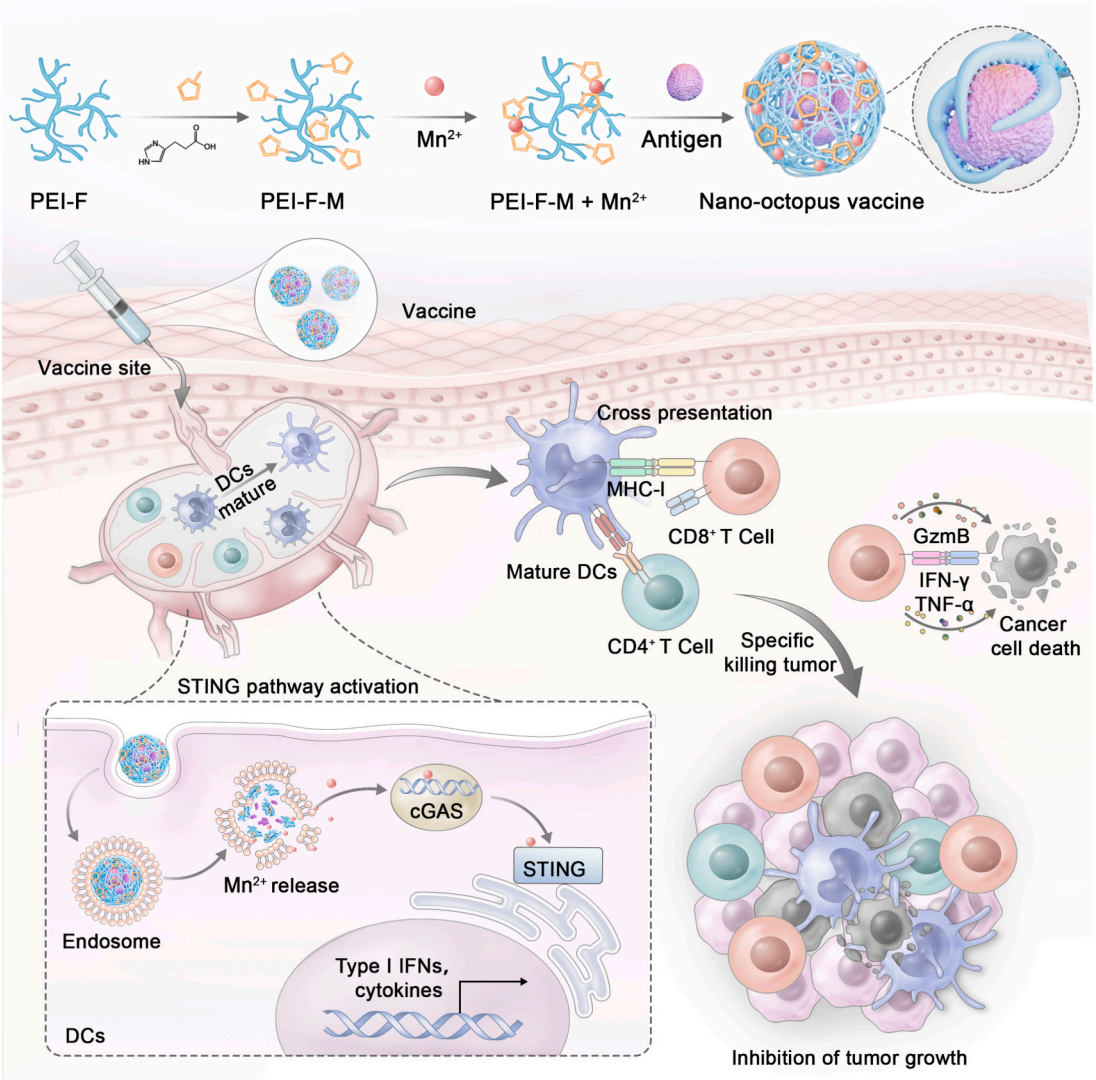


**Scheme 1.** Schematic illustration of octopus inspired vaccine design to overcome multiple barriers in antigen delivery. The nano-octopus vaccine captures antigens through PEI "tentacles" and imidazole-$Mn^{2+}$ "suction cups", enabling high antigen loading and efficient cytosolic delivery. It facilitates DC maturation, activates the STING pathway, and enhances antigen cross-presentation, ultimately eliciting strong $CD8^+$ T cell responses for tumor suppression.

## 2. Results and discussion

### 2.1. Characterization and cytosolic delivery study of nano-octopus vaccine

The nano-octopus vaccine was synthesized following the route illustrated in Fig. 1a. Initially, fluorinated polyethyleneimine (PEI-F) was synthesized based on previously reported protocols (Fig. S1, Supporting Information) [28]. Subsequently, imidazole-functionalized PEI-F (designated as PEI-F-M) was obtained by grafting 3-(imidazol-4-yl) propionic acid onto PEI-F via amide bond formation. $^1$H NMR analysis confirmed the successful introduction of approximately 25 imidazole moieties per PEI-F molecule (Fig. S2, Supporting Information). PEI-F-M was then dissolved in methanol and mixed with an aqueous solution of $MnCl_2$. After vortexing, stirring, and sonication, manganese-loaded PEI-F-M (PEI-F-M + $Mn^{2+}$) was obtained through coordination between $Mn^{2+}$ ions and imidazole groups. For comparison, imidazole-modified PEI (PEI-M) was synthesized using the same method and used to prepare PEI-M + $Mn^{2+}$ nanoparticles (Fig. S3, Supporting Information). Elemental analysis showed that the $Mn^{2+}$ contents in PEI-F-M + $Mn^{2+}$ and PEI-M + $Mn^{2+}$ were 1.9% and 2.9% (*w*/w), respectively (Table S1, Supporting Information). The resulting materials were then physically mixed with the model antigen ovalbumin (OVA) at a 1:1 (w/w) to generate the corresponding nanovaccine.

The physicochemical characteristics of the nanovaccine were evaluated using dynamic light scattering (DLS) and transmission electron microscopy (TEM). DLS analysis revealed that PEI-M + $Mn^{2+}$, PEI-F-M, and PEI-F-M + $Mn^{2+}$ all formed uniform nanostructures with OVA, with average hydrodynamic diameters around 200 nm (Fig. 1b, Fig. S4, Supporting Information). Zeta potential measurements indicated that all nanovaccine possessed positively charged surfaces, with values ranging from +27.2 mV to +33.6 mV (Fig. S5, Supporting Information). Additionally, no significant aggregation was observed in 50% FBS, confirming the stability of the nanovaccines under physiological conditions (Fig. S6, Supporting Information).

To quantitatively assess antigen loading efficiency, OVA was labeled with fluorescein isothiocyanate (OVA-FITC), and unbound antigen was removed by ultrafiltration. The results showed that PEI-F-M + $Mn^{2+}$ efficiently loaded OVA-FITC, achieving loading efficiency exceeding 95% and loading capacity of OVA-FITC was 47.8% (Fig. S7, Table S2, Supporting Information). To further assess the stabilizing effect of $Mn^{2+}$ on antigen loading, fluorescence spectroscopy was employed. It has been reported that the formation of stable polymer/protein nanoparticles often results in fluorescence quenching due to changes in the protein microenvironment [33]. As shown in Fig. 1c and Fig. S8 (Supporting Information), nanovaccine containing $Mn^{2+}$ (PEI-F-M + $Mn^{2+}$/OVA and PEI-M + $Mn^{2+}$/OVA) exhibited significantly reduced fluorescence intensity compared to their $Mn^{2+}$-free counterparts (PEI-F-M/OVA and PEI-M/OVA), indicating that $Mn^{2+}$ plays a key role in stabilizing the polymer-protein complex. $Mn^{2+}$ release from the nanovaccine is pH-dependent, with significantly higher release at acidic pH (Fig. S9, Supporting Information). Fluorescent labeling studies further confirmed the broad-spectrum protein loading capacity of PEI-F-M + $Mn^{2+}$. Fluorescent labeling studies further confirmed the broad-spectrum protein-loading capacity of PEI-F-M + $Mn^{2+}$, with consistently high loading efficiencies observed for various model proteins, including HAS-FITC, BSA-FITC, and BSA-RBITC, mirroring the results obtained for OVA-FITC (Fig. 1d). Notably, PEI-F-M + $Mn^{2+}$ exhibited loading efficiencies above 95.0% for OVA, HAS, and BSA, regardless of differences in their isoelectric points or molecular weights. These results demonstrate the significant antigen-loading capacity of PEI-F-M + $Mn^{2+}$ through octopus inspired design: the flexible PEI backbone acts as tentacle-like arms, while the imidazole-$Mn^{2+}$ coordination units resemble suction cups, enabling multivalent interactions (electrostatic, coordination, and hydrophobic) for stable and efficient protein capture.

Efficient APC uptake and cytosolic delivery of vaccine is critical for the activation of T cell-mediated immune responses [34,35]. We first assessed the cytotoxicities of polymer vaccines in DC2.4 cells using the Cell Counting Kit-8 (CCK-8) assay (Fig. 1e). Cell viability remained above 80% at concentrations below 20 μg/mL and such dose was used in subsequent experiments. DC2.4 cells were incubated with OVA-FITC-loaded nanovaccine for 8 h, and cellular uptake was visualized by confocal laser scanning microscopy (CLSM). As shown in Fig. 1f, both PEI-F/OVA and PEI-F-M + $Mn^{2+}$/OVA groups exhibited significantly enhanced fluorescence signals in the cytoplasmic region compared to the free OVA-FITC group. In contrast, the fluorescence signal of free OVA-FITC overlapped extensively with Lyso-Tracker Red, a commercial probe for lysosomes, indicating that most of the antigen remained trapped in lysosomes. Co-localization analysis using ImageJ software revealed that the Pearson's correlation coefficients between OVA-FITC and Lyso-Tracker Red in the PEI-F/OVA and PEI-F-M + $Mn^{2+}$/OVA groups were significantly lower than that in the free OVA group (Fig. 1g), further confirming the superior cytosolic delivery capacity of the nano-octopus vaccine.

Flow cytometry (FCM) was subsequently employed to quantitatively assess cytosolic delivery efficiency. As shown in Fig. 1h, the nano-octopus vaccine significantly enhanced OVA-FITC uptake by DC2.4 cells compared to free OVA. Moreover, the cellular uptake increased over time and reached saturation at approximately 12 h (Fig. 1i). The internalization of the nanovaccine is inhibited by 5-(N-Ethyl-N-isopropyl)amiloride (EIPA) treatment, indicating that the nanovaccine may enter cells via macropinocytosis. (Fig. S10, Supporting Information). The PEI-F-M + $Mn^{2+}$/OVA nanovaccine utilizes the proton sponge effect in acidic endosomes, where the fluorinated polymer captures protons, causing osmotic swelling and rupture of the endosomal membrane, facilitating OVA release into the cytosol. The imidazole modification does not interfere with this process, and the enhanced buffering capacity of fluorinated PEI ensures efficient antigen delivery without affecting release efficiency.

### 2.2. Nano-octopus vaccine promotes DC maturation and activates STING signaling pathway in vitro

To evaluate the immunomodulatory properties of the nanovaccine, we assessed the ability of design vaccines to activate APCs, a process that plays a central role in orchestrating adaptive immune responses [36,37]. Bone marrow-derived dendritic cells (BMDCs) were incubated with different nanovaccine formulations for 24 h, followed by FCM analysis of key DC maturation markers, including CD40, CD86, and MHC II (Fig. 2a). As shown in Fig. 2b-d and Figs. S11–14 (Supporting Information), the PEI-F-M + $Mn^{2+}$/OVA nanovaccine significantly upregulated the expression of CD40 and CD86 compared to other groups. Notably, CD40 expression in the PEI-F-M + $Mn^{2+}$/OVA group was 5.8-fold higher than in the untreated control and 1.4 times that of the PEI-F/OVA group. Moreover, MHC II expression in the PEI-F-M + $Mn^{2+}$/OVA group was 1.9 times that in free OVA group. To further assess the antigen cross-presentation capability of DCs, the expression of SIINFEKL-H-2Kb complexes on the surface of BMDCs was quantified using FCM (Figs. S15, S16, Supporting Information). The PEI-F-M + $Mn^{2+}$/OVA group exhibited nearly twice the SIINFEKL-H-2Kb expression level observed in the free OVA group (Fig. 2e), indicating that the nanovaccine effectively enhances antigen processing and cross-presentation of BMDCs.

Given the observed cytosolic delivery and DC activation, we next explored whether the STING signaling pathway was involved. STING serves as a pivotal regulator of innate immunity, and $Mn^{2+}$ has been reported as a metal-based immune adjuvant capable of enhancing APC function through STING activation [38,39]. We hypothesized that the PEI-F-M + $Mn^{2+}$/OVA vaccine not only promotes efficient antigen uptake and processing by DCs, but also facilitates intracellular release of $Mn^{2+}$, thereby triggering STING pathway activation and upregulating the phosphorylation of its downstream signaling molecules, including

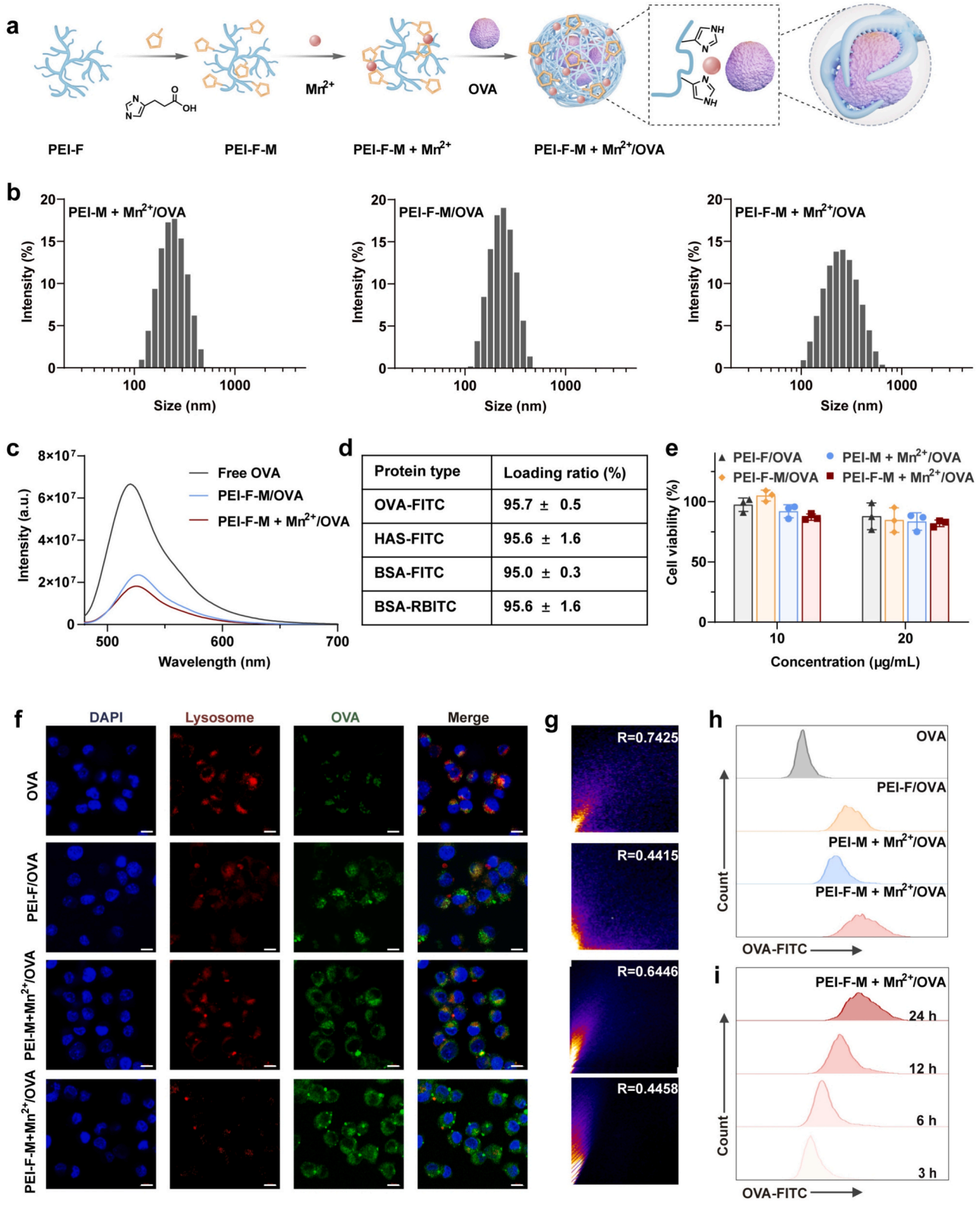


**Fig. 1.** Synthesis, physicochemical characterization, and cytosolic delivery efficiency of the nano-octopus vaccine. (a) Schematic illustration of the stepwise preparation of the nano-octopus vaccine. (b) Hydrodynamic size distribution of the nanovaccine measured by DLS. (c) Fluorescence spectra of PEI-F-M/OVA and PEI-F-M + $Mn^{2+}$/OVA formulations in physiological saline. (d) Protein loading efficiencies of PEI-F-M + $Mn^{2+}$ for different proteins. (e) Cell viability of DC2.4 cells after 24 h treatment with different nanovaccine formulations assessed by CCK-8 assay. (f) Confocal laser scanning microscopy (CLSM) images of DC2.4 cells after incubation with OVA-FITC-loaded nanovaccine for 8 h. Scale bar: 10 μm. (g) Quantification of co-localization between OVA-FITC and lysosomes (LysoTracker Red) analyzed using ImageJ software. (h) Flow cytometric analysis of cellular uptake after 24 h incubation with various OVA-FITC labeled nanovaccine. (i) Time-dependent internalization profile of PEI-F-M + $Mn^{2+}$/OVA nanovaccine by DC2.4 cells. All data are presented as mean ± standard deviation (SD) from at least three independent experiments ($n = 3$). (For interpretation of the references to colour in this figure legend, the reader is referred to the web version of this article.)

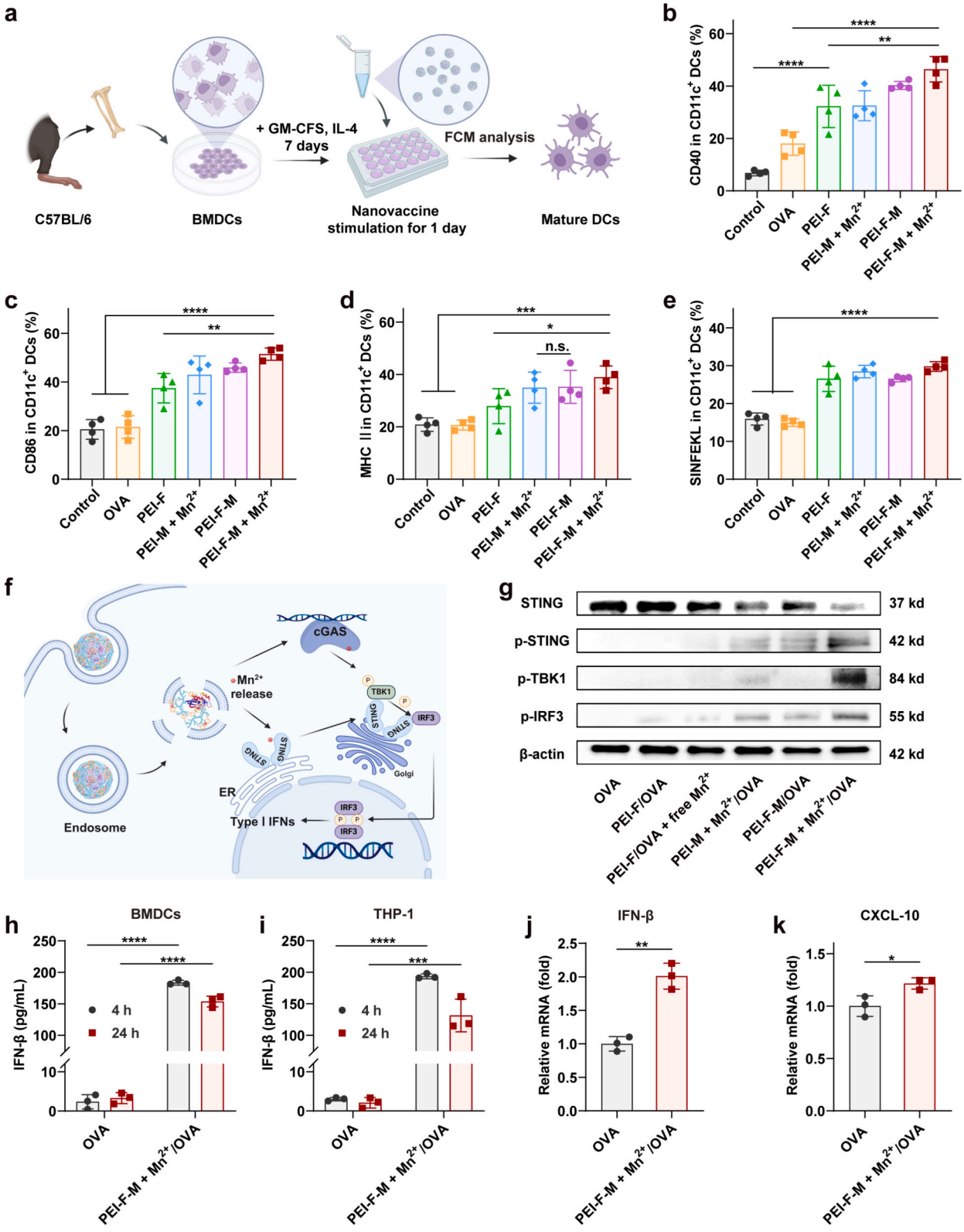


**Fig. 2.** Nano-octopus vaccine promotes DC maturation, enhances antigen cross-presentation, and activates the STING signaling pathway. (a) Schematic illustration of BMDC maturation induced by the nanovaccine. (b-e) Flow cytometry (FCM) analysis of BMDCs after 24 h incubation with different nanovaccine formulations, quantifying the expression of maturation markers CD40 (b), CD86 (c), MHC II (d), and the proportion of antigen cross-presentation (SIINFEKL-H-2Kb) (e) in $CD11c^+$ dendritic cells ($n = 4$). (f) Proposed mechanism of STING activation by the nano-octopus vaccine. (g) Western blot analysis of phosphorylated proteins (p-STING, p-TBK1, and p-IRF3) in THP-1 cells after 24 h treatment with different nanovaccine formulations. (h, i) IFN-β secretion levels measured by ELISA in BMDCs (h) and THP-1 cells (i) after 4 h and 24 h co-incubation with nanovaccine. (j, k) mRNA expression levels of IFN-β (j) and CXCL10 (k) in THP-1 cells after 24 h treatment, determined by qPCR ($n = 3$). Statistical significance among multiple groups was determined by one-way analysis of variance (ANOVA) with Tukey's post hoc test. Comparisons between two groups were performed using a two-tailed Student's *t*-test. n.s.: not significant, $*p < 0.05$; $**p < 0.01$; $***p < 0.001$; $****p < 0.0001$.

TANK-binding kinase 1 (TBK1) and interferon regulatory factor 3 (IRF3) (Fig. 2f). To validate this, we conducted Western blotting (WB) analysis to assess the phosphorylation levels of key STING pathway proteins in THP-1 cells after 24 h treatment with various nanovaccine formulations. As shown in Fig. 2g, the PEI-F-M + $Mn^{2+}$/OVA group significantly increased phosphorylation of STING (p-STING), TBK1 (p-TBK1), and IRF3 (p-IRF3) relative to both the control and free $Mn^{2+}$ groups, confirming robust activation of the STING pathway. Furthermore, enzyme-linked immunosorbent assay (ELISA) results revealed that PEI-F-M + $Mn^{2+}$/OVA treatment induced significantly higher IFN-β secretion in THP-1 cells, with a similar trend observed in BMDCs (Figs. 2h, i). Quantitative real-time PCR (qPCR) analysis also demonstrated markedly elevated mRNA expression of IFN-β and CXCL10 in the PEI-F-M + $Mn^{2+}$/OVA group compared to the free OVA group (Fig. 2j, k). Collectively, these results demonstrate that the nano-octopus vaccine enhances antigen uptake, cytosolic delivery, and cross-presentation in DCs while simultaneously activating the STING signaling pathway. This synergistic mechanism potentiates both antigen processing and immune activation, establishing a robust platform for immunoenhancement.

### 2.3. Evaluation of the immune effect of nano-octopus vaccine in vivo

To assess the immune efficacy of the nanovaccine in vivo, we first examined DC activation in draining lymph nodes (DLNs). C57BL/6 mice were immunized via subcutaneous injection, and after 3 days, draining lymph nodes (DLNs) were collected for DC maturation and antigen cross-presentation analysis by FCM (Fig. 3a). The expression levels of co-stimulatory molecules CD40 and CD86 on $CD11c^+$ DCs were significantly elevated in the PEI-F-M + $Mn^{2+}$/OVA group, indicating effective DC maturation (Fig. 3b, c). Additionally, the expression of MHC II on DCs in the PEI-F-M + $Mn^{2+}$/OVA group was 1.88 times that of the free OVA group, suggesting enhanced antigen-presenting capability (Fig. 3d). Notably, the PEI-F-M + $Mn^{2+}$/OVA group exhibited the highest expression of SIINFEKL-H-2Kb in the DLNs, demonstrating enhanced antigen cross-presentation (Fig. 3e). $Mn^{2+}$ activates the STING pathway, enhancing DC maturation and antigen cross-presentation through cytosolic antigen delivery. These in vivo results align with our in vitro findings, further confirming that the PEI-F-M + $Mn^{2+}$/OVA nanovaccine effectively promotes DC maturation and antigen cross-presentation.

Subsequently, we evaluated the nanovaccine's retention in DLNs. OVA was labeled by Cy5 fluorescent dye (OVA-Cy5) and the nanovaccine was administered into mice via intradermal injection. After 24 h, fluorescence signals in the DLNs from various groups were measured using an in vivo imaging system (Lumina IVIS) (Fig. 3a). The PEI-F-M + $Mn^{2+}$/OVA group (G7) displayed markedly stronger fluorescence signals compared to the free OVA group (G2), indicating enhanced antigen retention in the lymph nodes (Fig. 3f). Quantitative analysis confirmed that the fluorescence intensity of the PEI-F-M + $Mn^{2+}$/OVA group was 5.2 times that of the free OVA group and 1.6 times that of the PEI-F/OVA group (Fig. 3g).

We next investigated antigen-specific T cell responses induced by the nanovaccine. Mice were subcutaneously immunized on days 0 and 14, and splenocytes were harvested on day 21 for flow cytometric analysis (Fig. 3h). Upon stimulation with the SIINFEKL peptide ($OVA_{257–264}$ peptide), $CD8^+$ T cells from the PEI-F-M + $Mn^{2+}$/OVA group secreted significantly higher levels of IFN-γ and TNF-α compared to the free OVA group, indicating robust cytotoxic T cell responses (Fig. 3i and Figs. S17–19, Supporting Information). Consistently, ELISA results showed that serum IFN-γ levels were highest in the PEI-F-M + $Mn^{2+}$/OVA group (Fig. 3j). Moreover, $CD4^+$ T cells in the PEI-F-M + $Mn^{2+}$/OVA group produced significantly greater amounts of IFN-γ and IL-2 upon OVA stimulation than those in other groups, suggesting potent induction of helper T cell responses (Figs. S20–22, Supporting Information). To further evaluate the magnitude of antigen-specific T cell responses, enzyme-linked immunospot (ELISPOT) assays were performed to quantify the frequency of IFN-γ secreting splenocytes (Fig. 3k, Fig. S23, Supporting Information). The PEI-F-M + $Mn^{2+}$/OVA group exhibited the highest number of IFN-γ spots, reflecting robust antigen-specific cellular immunity. Additionally, MHC-I tetramer staining confirmed the enhanced frequency of OVA-specific $CD8^+$ T cells induced by the nanovaccine. The frequency of tetramer-positive $CD8^+$ T cells in the PEI-F-M + $Mn^{2+}$/OVA group was significantly higher than that in the other groups, being 1.51-fold higher than in the PEI-F/OVA group (Fig. 3l, m). These findings demonstrate that the PEI-F-M + $Mn^{2+}$/OVA nanovaccine elicits potent antigen-specific T cell responses in vivo.

Finally, a cytotoxic T lymphocyte (CTL) killing assay was conducted to validate the functional cytotoxicity of the immune response. High-concentration CFSE-labeled cells ($CFSE^{high}$) stimulated with the SIINFEKL peptide and low-concentration CFSE-labeled cells ($CFSE^{low}$) without peptide stimulation were mixed and intravenously injected into mice that had received two rounds of vaccination. After 18 h, the proportion of $CFSE^{high}$ and $CFSE^{low}$ cells in splenocytes was analyzed by FCM (Fig. 3n). The proportion of $CFSE^{high}$ cells in the PEI-F-M + $Mn^{2+}$/OVA group was significantly reduced, indicating superior antigen-specific cytotoxic activity (Fig. 3o, p). This further demonstrates that the PEI-F-M + $Mn^{2+}$/OVA nanovaccine effectively enhances antigen-specific CTL responses.

### 2.4. Evaluation of in vivo antitumor efficacy of the nano-octopus vaccine

To further evaluate the antitumor efficacy of the nanovaccine, a B16-OVA tumor model was employed. The tumor model was established by subcutaneously injecting $2 \times 10^5$ B16-OVA cells into the right flank of female C57BL/6 mice (Fig. 4a). Tumor-bearing mice were then randomly assigned to five experimental groups: PBS control group (G1), free OVA group (G2), PEI-F/OVA group (G3), PEI-M + $Mn^{2+}$/OVA group (G4), and PEI-F-M + $Mn^{2+}$/OVA group (G5). Each group received four subcutaneous vaccinations near the left inguinal lymph node on days 3, 7, 11, and 15. Compared to the free OVA group, which showed no significant tumor inhibition, the PEI-F-M + $Mn^{2+}$/OVA group exhibited the most pronounced antitumor effect, resulting in a tumor inhibition rate of 88.1% on day 18 (Fig. 4b, c). Biodistribution and safety assessments revealed no histopathological abnormalities or significant body weight changes in any experimental groups, confirming the favorable safety profile of the PEI-F-M + $Mn^{2+}$/OVA nanovaccine (Figs. S24–26, Supporting Information). Moreover, survival analysis revealed that the mice injected with the PEI-F-M + $Mn^{2+}$/OVA nanovaccine exhibited the longest survival time (Fig. S27, Supporting Information).

To explore the immune mechanisms underlying the antitumor effect, we analyzed its impact on $CD8^+$ T cells and the expression of their cytotoxic mediators. In tumor tissues from the PEI-F-M + $Mn^{2+}$/OVA group, the proportion of $CD8^+$ T cells was 1.83-fold higher than that in the free OVA group (Fig. 4d, Fig. S28, Supporting Information). Further FCM analysis revealed that $CD8^+$ T cells from the PEI-F-M + $Mn^{2+}$/OVA group showed significantly increased expression of granzyme B (GZMB), IFN-γ, and TNF-α (Fig. 4e-g, Figs. S29, S30, Supporting Information). ELISA confirmed that the levels of these cytokines in the tumor tissue of the PEI-F-M + $Mn^{2+}$/OVA group were significantly higher than in the other groups, indicating that the nanovaccine substantially enhanced the cytotoxic activity of $CD8^+$ T cells (Fig. 4h-j).

Simultaneously, we assessed the maturation status of DCs in the lymph nodes was evaluated. FCM analysis showed the proportion of mature DCs in the PEI-F-M + $Mn^{2+}$/OVA group was the highest compared to other groups (Fig. 4k, Figs. S31, S32, Supporting Information). In addition, the PEI-F-M + $Mn^{2+}$/OVA nanovaccine further enhanced the antitumor immune response by modulating immunosuppressive cells within the tumor microenvironment (Fig. 4l, m). The proportion of regulatory T cells (Tregs, $CD25^+Foxp3^+$ phenotype) and myeloid-derived suppressor cells (MDSCs, $Gr1^+CD11b^+$ phenotype) in the PEI-F-M + $Mn^{2+}$/OVA group were lower than those in other groups.

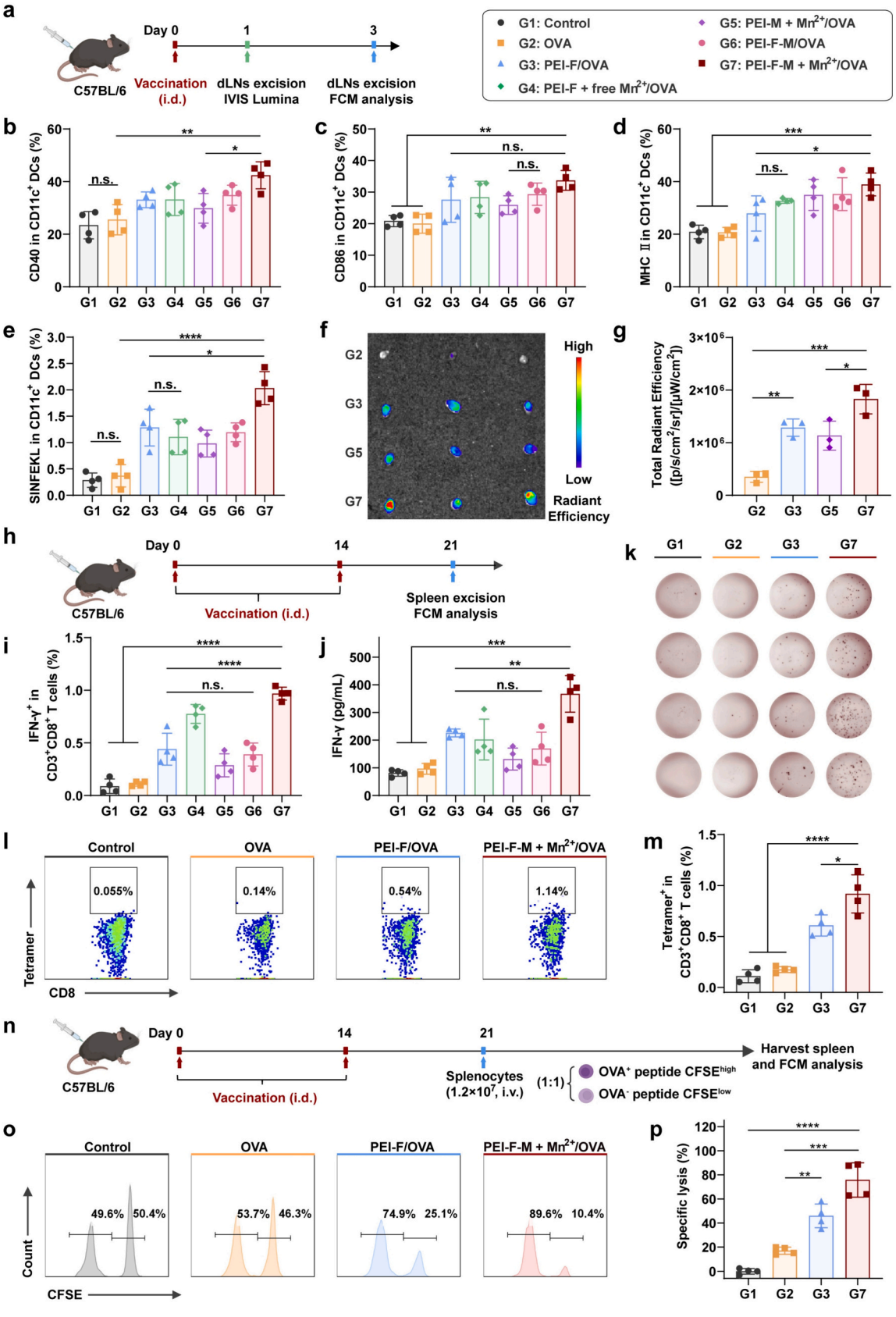


*(caption on next page)*

**Fig. 3.** Immune activation induced by nano-octopus vaccine in vivo. (a) Schematic representation of the experimental design used to evaluate immune response activated in draining lymph nodes (DLNs) by nanovaccine. (b-d) Proportion of CD40, CD86, and MHC II expression of $CD11c^+$ DCs in DLNs three days post-immunization with various nanovaccine. (e) Proportion of SIINFEKL peptide presentation in $CD11c^+$ DCs. (f, g) Accumulation of nanovaccine in DLNs and quantitative analysis of fluorescence intensity for different formulations ($n = 3$). (h) Schematic representation of the experimental design used to evaluate immune response activated in spleen by nanovaccine. (i) Proportion of IFN-$\gamma^+$ $CD8^+$ T cells after SIINFEKL peptide stimulation for 6 h ($n = 4$). (j) ELISA quantification of IFN-γ concentration in splenocyte culture supernatants ($n = 4$). (k) ELISPOT assay showing the number of IFN-γ secretion spots induced by SIINFEKL peptide stimulation of splenocytes for 24 h (n = 4). (l, m) Representative FCM dot plots and statistical analysis of the frequency of MHC-I tetramer-positive OVA-specific $CD8^+$ T cells ($n = 4$). (n) Schematic illustration of the antigen-specific cytotoxicity assay. (o, p) Representative FCM dot plots and statistical analysis of the specific killing percentage of CFSE-labeled target cells. Statistical significance among multiple groups was determined by ANOVA with Tukey's post hoc test. n.s.: not significant, $*p < 0.05$; $**p < 0.01$; $***p < 0.001$; $****p < 0.0001$.

(Figs. S33–36, Supporting Information). Moreover, the proportions of central memory T cells ($T_{CM}$, $CD44^+CD62L^+$ phenotype) and effector memory T cells ($T_{EM}$, $CD44^+CD62L^-$ phenotype) in the spleen of PEI-F-M + $Mn^{2+}$/OVA group were higher than those in other groups. (Fig. 4n-o, Figs. S37, 38, Supporting Information), suggesting that the vaccine has the potential to induce long-term immune memory. Overall, these results indicate the immunosuppressive environment and further activates the antitumor activity of effector T cells. In summary, the PEI-F-M + $Mn^{2+}$/OVA nanovaccine effectively achieves significant antitumor effects through multiple immune mechanisms.

### 2.5. Inhibition of melanoma lung metastasis by the nano-octopus vaccine

To investigate the effect of the nanovaccine on metastatic inhibition, a B16-OVA lung metastasis model was established to mimic the dissemination of melanoma cells. As shown in Fig. 5a, lung metastases were induced by intravenous injection of $2 \times 10^5$ B16-OVA melanoma cells into C57BL/6 mice on Day 0. The tumor-bearing mice were randomly assigned to four groups: Control, OVA, PEI-F/OVA, and PEI-F-M + $Mn^{2+}$/OVA. Each group was subcutaneously vaccinated near the right inguinal lymph node on days 3, 7, 11, and 15. Survival analysis showed that mice in the control group began to die on Day 22, with all animals succumbing by Day 34. In contrast, mice treated with the PEI-F-M + $Mn^{2+}$/OVA nanovaccine exhibited significantly prolonged survival, demonstrating clear advantages over both the OVA and PEI-F/OVA groups (Fig. 5b). Moreover, analysis of OVA-specific tetramer-positive $CD8^+$ T cells in splenocytes revealed that the PEI-F-M + $Mn^{2+}$/OVA group had the highest proportion of these cells, significantly exceeding levels observed in the other groups (Fig. 5c, d). These results indicate that the nanovaccine induces a robust OVA-specific $CD8^+$ T cell immune response.

In the metastasis inhibition studies, the number of lung metastatic nodules in the PEI-F-M + $Mn^{2+}$/OVA group was significantly lower than that in the other groups (Fig. 5e). H&E staining further confirmed that while the control group exhibited numerous metastatic lesions in the lung tissue, the lungs of mice in the PEI-F-M + $Mn^{2+}$/OVA group showed almost no visible metastatic lesions (Fig. 5f). Quantitative analysis revealed an 82.2% inhibition rate of lung metastases in the PEI-F-M + $Mn^{2+}$/OVA group compared to the control group (Fig. 5g). Taken together, the PEI-F-M + $Mn^{2+}$/OVA nanovaccine significantly inhibits melanoma lung metastasis and extends survival by enhancing the antigen-specific $CD8^+$ T cell response, demonstrating substantial potential for combating tumor metastasis.

### 2.6. Universal anti-tumor effects of the nano-octopus vaccine

The therapeutic potential and universality of the nano-octopus vaccine was further investigated on a human papillomavirus (HPV) E6/E7 TC-1 tumor model in comparison to commercial adjuvant CpG. The TC-1 tumor model, based on TC-1 cells expressing the HPV16 E7 protein, holds significant clinical relevance [40,41]. The TC-1 tumor model was established by subcutaneously injecting $2.5 \times 10^5$ TC-1 cells into the right flank of female C57BL/6 mice. The HPV-derived E7 peptide-loaded nanovaccine was then prepared as per the established protocol. On days 3, 7, 11, and 14 after tumor inoculation, mice were subcutaneously injected with PBS, free E7 peptide, free E7 peptide combined with CpG adjuvant, or PEI-F-M + $Mn^{2+}$/E7 nanovaccine (Fig. 6a). The PEI-F-M + $Mn^{2+}$/E7 nanovaccine significantly inhibited tumor growth, exhibiting superior efficacy compared to both free E7 peptide and free E7 peptide combined with CpG adjuvant groups (Fig. 6b). Compared to the control group, mice in the PEI-F-M + $Mn^{2+}$/E7 nanovaccine group exhibited a marked reduction in tumor volume and a significant slowing of tumor growth (Fig. 6c). Throughout the experiment, no significant weight changes were observed in treated groups, confirming the favorable safety profile of the nanovaccine (Fig. S39, Supporting Information). Additionally, mice treated with PEI-F-M + $Mn^{2+}$/E7 nanovaccine showed a significantly extended survival time, with no deaths within 48 days and 100%of mice surviving beyond 70 days (Fig. 6d).

Flow cytometric analysis of DC activation in the DLNs revealed that the PEI-F-M + $Mn^{2+}$/E7 nanovaccine significantly increased DC activation compared to other groups (Fig. 6e, f). This enhanced antigen presentation capability further promoted the expansion of $CD8^+$ T cells (Fig. 6g). These results indicate that the PEI-F-M + $Mn^{2+}$/E7 nanovaccine effectively suppresses tumor growth by enhancing antigen presentation and $CD8^+$ T cell activation.

To assess the immunological memory induced by the PEI-F-M + $Mn^{2+}$/E7 nanovaccine, a rechallenge experiment was performed using mice that survived during the initial treatment. The results showed that mice treated with the nanovaccine exhibited no tumor growth after re-challenge with TC-1 cells, indicating that the vaccine successfully induced durable anti-tumor immune memory (Fig. 6h). Peripheral blood mononuclear cell analysis further showed that, in the PEI-F-M + $Mn^{2+}$/E7 nanovaccine-treated group, the proportion of $T_{EM}$ and $T_{CM}$ cells within $CD3^+CD8^+$ T cells was significantly higher (Fig. 6i-k), with a similar trend was observed in $CD3^+CD4^+$ T cells (Fig. 6l, m, Fig. S40, Supporting Information). These results suggest that the PEI-F-M + $Mn^{2+}$/E7 nanovaccine not only effectively activates tumor-specific cytotoxic T cells but also enhances the immune memory and function of helper T cells. Furthermore, flow cytometric analysis of IFN-γ and IL-2 levels in $CD8^+$ and $CD4^+$ T cells revealed significantly increased expression of these cytokines in the peripheral blood of mice treated with the PEI-F-M + $Mn^{2+}$/E7 nanovaccine (Fig. 6n, o). These findings indicate that the PEI-F-M + $Mn^{2+}$/E7 nanovaccine effectively activates antitumor immune response. In conclusion, the nano-octopus vaccine platform demonstrates broad applicability, providing substantial potential for expanding the scope of cancer immunotherapy.

## 3. Methods

### 3.1. Synthesis of PEI-F-M + $Mn^{2+}$

First, fluorinated polyethyleneimine (PEI-F) was synthesized based on previously reported protocols [28]. Imidazole-modified PEI-F (PEI-F-M) was synthesized using an EDC·HCl/NHS coupling method with a grafting degree of 25. Briefly, 3-(imidazol-4-yl)propionic acid (25 eq, 10.29 mg), EDC·HCl (60 eq, 33.80 mg), and NHS (80 eq, 27.05 mg) were dissolved in dimethyl sulfoxide (DMSO) and activated for 30 min. PEI-F (100 mg) was then added to the mixture, and the reaction was allowed to proceed at 30 °C for 72 h. The product was characterized by $^1H$ NMR. In addition, PEI-M was prepared using the same EDC·HCl/NHS coupling

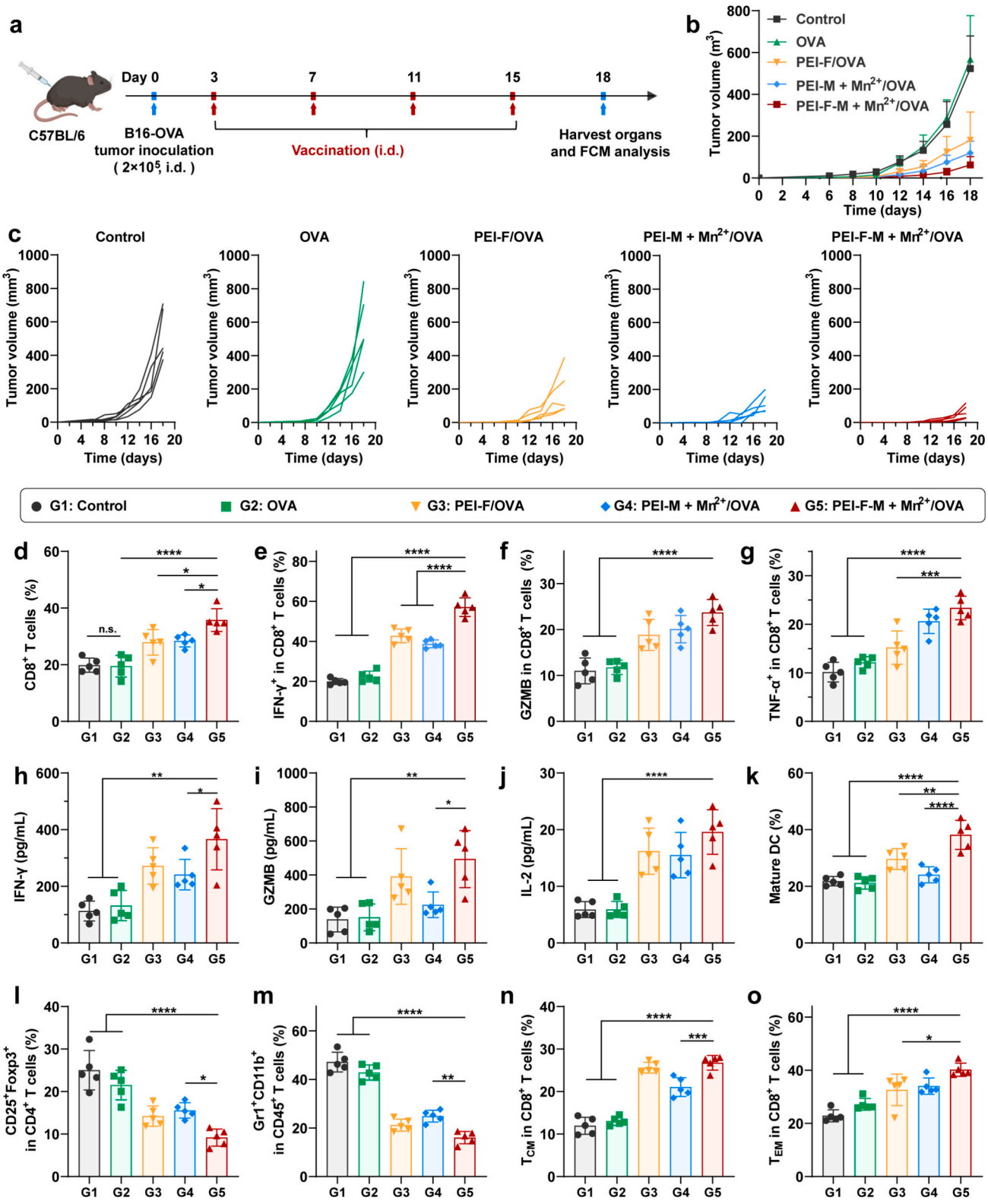


**Fig. 4.** Therapeutic effects of the nano-octopus vaccine in B16-OVA melanoma. (a) Schematic representation of vaccination and treatment for B16-OVA melanoma. (b) Average tumor growth curves for each treatment group after vaccination. (c) Individual tumor growth curves for different treatment group after vaccination. (d) Proportion of $CD8^+$ T cells in tumors from each group. (e-g) Proportion of IFN-$\gamma^+CD8^+$, $GZMB^+CD8^+$, TNF-$\alpha^+CD8^+$ in tumors from each group. (h-j) Levels of IFN-γ, GZMB, and IL-2 in tumor tissues measured by ELISA. (k) Statistical analysis of the proportion of mature DCs in tumors from each group. (l) Statistical analysis of the proportion of $CD25^+Foxp3^+$ in $CD4^+$ T cells in tumors from each group. (m) Statistical analysis of the proportion of $Gr1^+CD11b^+$ in $CD45^+$ cells in tumors from each group. (n, o) Statistical graphs of the proportion of effector memory T cells ($T_{EM}$) and central memory T cells ($T_{CM}$) memory cells in splenocytes of each group of mice. Statistical significance among multiple groups was determined by ANOVA with Tukey's post hoc test. $n = 5$; $^*p < 0.05$; $^{**}p < 0.01$; $^{***}p < 0.001$.

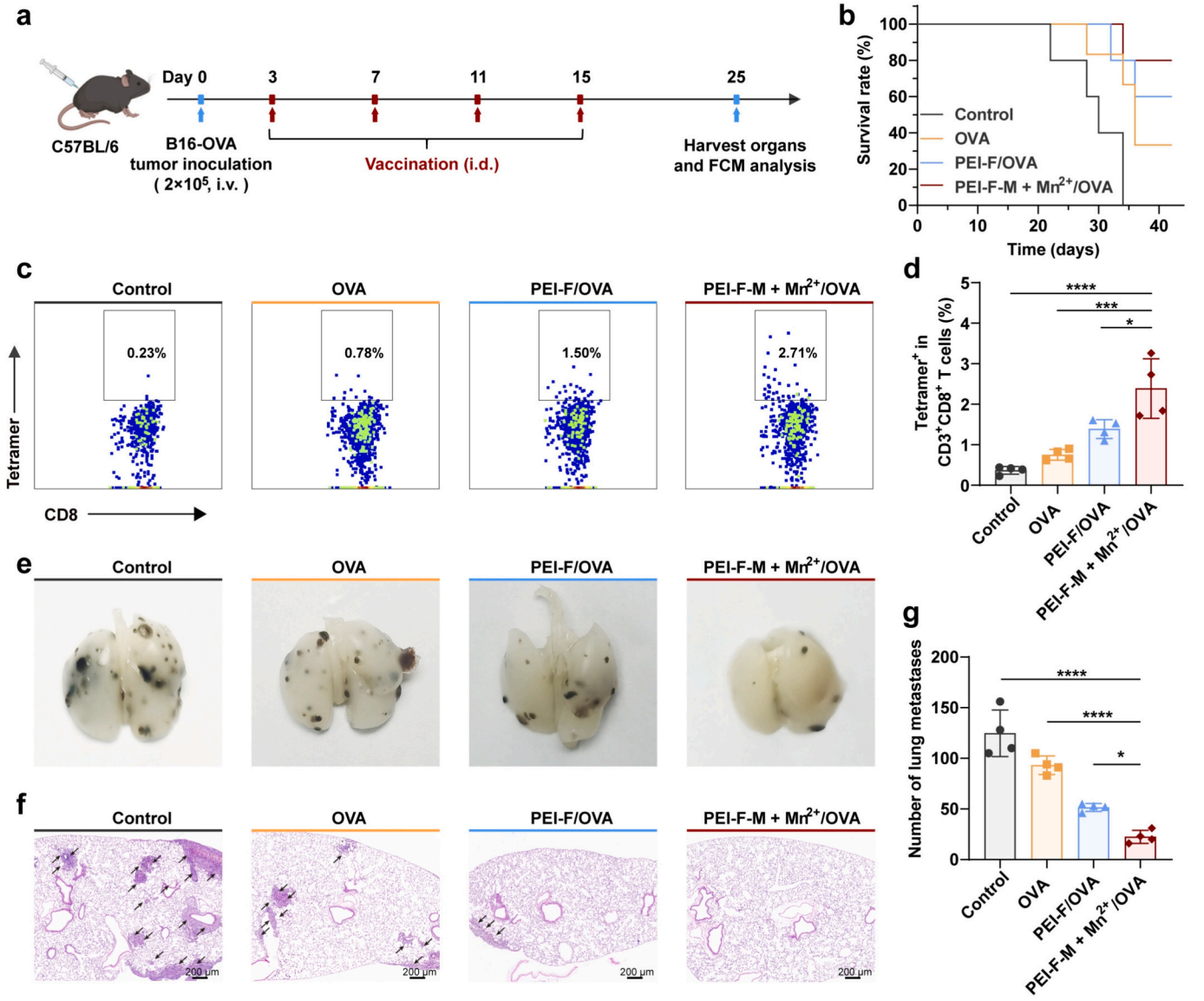


**Fig. 5.** Therapeutic effect of the nano-octopus vaccine against B16-OVA lung metastasis. (a) Schematic representation of vaccine administration and treatment schedule for B16-OVA lung metastasis. (b) Survival curves of different treatment groups. (c, d) Representative FCM plots and quantification of OVA-specific tetramer-positive $CD8^+$ T cells in splenocytes. (e, f) Lung tissues and corresponding H&E-stained sections from each group (scale bar = 200 μm). (g) Number of metastases of mice treated with different treatments. Survival curves were generated using the Kaplan-Meier method and compared using the Log-rank test to assess the differences between groups. Statistical significance among multiple groups was determined by one-way ANOVA with Tukey's post hoc test. $n = 4$; $^*p < 0.05$; $^{***}p < 0.001$; $^{****}p < 0.0001$.

strategy as described above, with varying degrees of imidazole modification.

To prepare $Mn^{2+}$-loaded polymer, PEI-F-M was first dissolved in methanol at a concentration of 1 mg/mL. A stock solution of $MnCl_2$ (100 mM in methanol) was then added dropwise at a molar ratio of 10:1 ($Mn^{2+}$: Imidazole groups). The mixture was vortexed, followed by brief sonication (1 min), and subsequently stirred at room temperature for 1 h to ensure complete coordination. The resulting PEI-F-M + $Mn^{2+}$ complex was washed thoroughly with methanol and purified by dialysis to remove unbound ions and solvents.

### 3.2. Evaluation of cytosolic delivery of nanovaccine

To evaluate endosomal escape efficiency, nanovaccine was prepared by complexing synthesized polymers with FITC-labeled ovalbumin (OVA-FITC). DC2.4 cells were seeded at $2 \times 10^5$ cells per well in 24-well plates and cultured in complete PRMI-1640 medium for 12 h. Cells were then incubated with either free OVA-FITC or nanovaccine (20 μg/mL) for 8 h. After incubation, cells were washed three times with phosphate-buffered saline (PBS), stained with LysoTracker Red, and imaged using confocal laser scanning microscopy to assess intracellular distribution and endosomal escape.

### 3.3. Evaluation of cellular uptake of nanovaccine

DC2.4 cells were seeded at a density of $2 \times 10^5$ cells/mL in 24-well plates and treated with nanovaccine (20 μg/mL) for 24 h. For time-dependent uptake analysis, cells were incubated with PEI-F-M + $Mn^{2+}$/OVA nanovaccine for 3, 6, 12, and 24 h. Following incubation, cells were collected, washed three times with PBS, and analyzed by FCM to quantify the extent of nanoparticle internalization. All experiments were performed in triplicate.

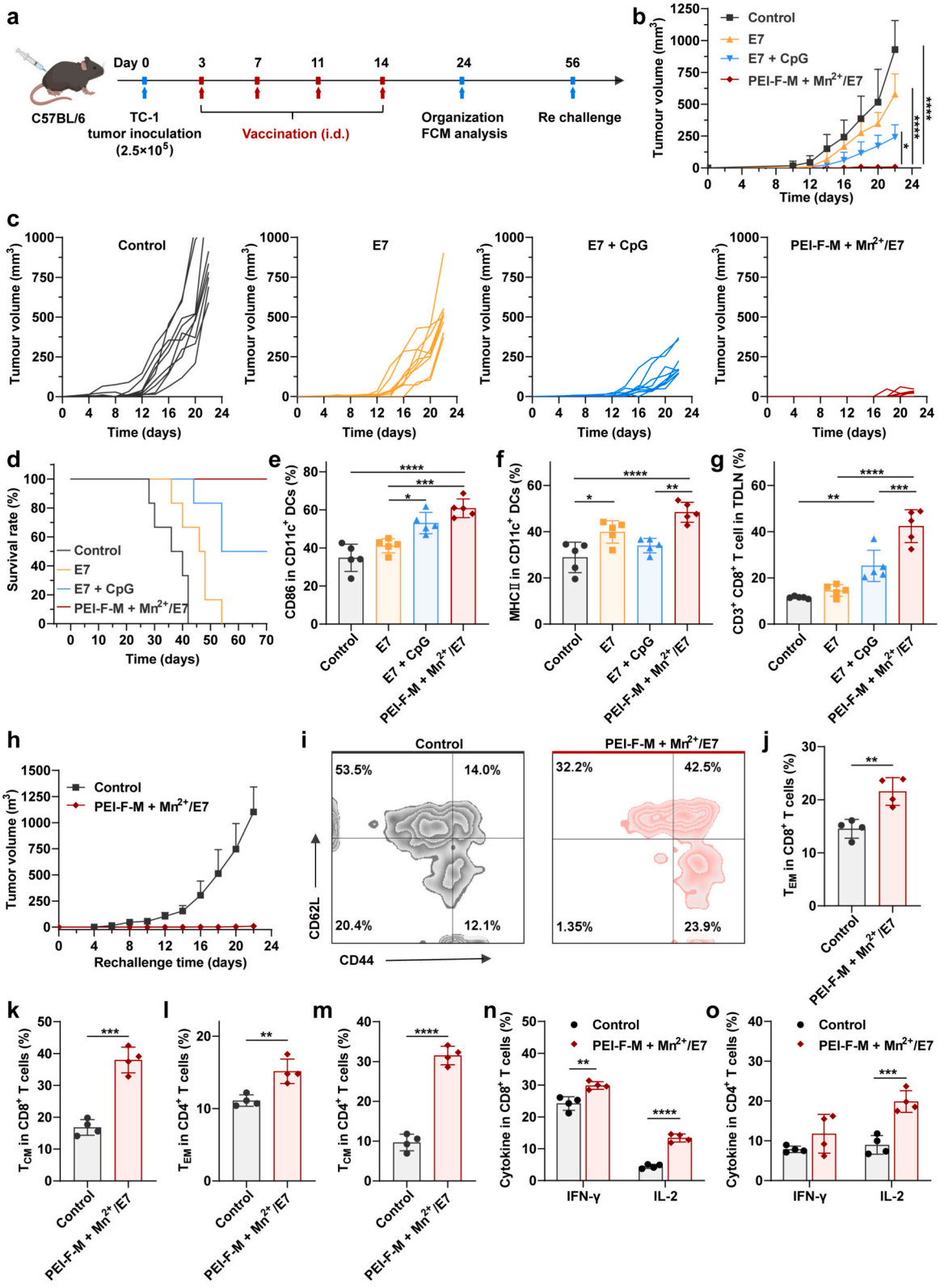


**Fig. 6.** Therapeutic efficacy of the nano-octopus vaccine in the TC-1 tumor model. (a) Schematic illustration of vaccination and treatment schedule with the nanovaccine in the TC-1 tumor model. (b) Average tumor growth curves in different groups. (c) Individual tumor growth curves for each mouse in different groups. (d) Survival curves in different groups. (e, f) Statistical analysis of the proportion of CD86 and MHC II expression in DLNs. (g) Proportion of $CD8^+$ T cells in $CD3^+$ T cells in tumor-DLNs (TDLNs). (h) Tumor volume curve of mice upon re-challenge with TC-1 tumor cells after vaccine treatment. (i) Representative FCM plots of memory cells among $CD8^+$ T cells in the blood of mice receiving the vaccine. (j, k) Statistical analysis of the proportion of $T_{CM}$ and $T_{EM}$ in $CD8^+$ T cells. (l, m) Statistical analysis of the proportion of $T_{CM}$ and $T_{EM}$ in $CD4^+$ T cells. (n) Proportion of IFN-γ and IL-2 in $CD8^+$ T cells. (o) The proportion of IFN-$\gamma^+$ and IL-$2^+$ in $CD4^+$ T cells. Statistical significance among multiple groups was determined by one-way ANOVA with Tukey's multiple comparisons test. Statistical significance between two groups was determined via two-tailed Student's *t*-test. $n = 4$, $^*p < 0.05$; $^{**}p < 0.01$; $^{***}p < 0.001$; $^{****}p < 0.0001$.

### 3.4. In vitro activation and cross-presentation of DCs

Bone marrow-derived dendritic cells (BMDCs) were isolated from C57BL/6 mice and cultured in RPMI-1640 medium supplemented with 20 ng/mL recombinant murine granulocyte-macrophage colony-stimulating factor (GM-CSF) and 10 ng/mL interleukin-4 (IL-4) at 37 °C with 5% $CO_2$. Half of the medium was refreshed on days 3 and 6 with fresh cytokine-supplemented medium. On day 7, non-adherent and loosely adherent BMDCs were harvested and plated at $2 \times 10^5$ cells per well in 24-well plates.

BMDCs were then treated with various formulations, including free OVA, PEI-F/OVA, PEI-M/OVA, PEI-M + $Mn^{2+}$/OVA, PEI-F-M/OVA, and PEI-F-M + $Mn^{2+}$/OVA for 24 h. After incubation, cells were washed with PBS and stained for flow cytometry analysis. Dead cells were excluded using Zombie Aqua™ viability dye. Surface markers for DC activation and antigen cross-presentation were detected using fluorochrome-conjugated antibodies against mouse CD11c, CD40, CD86, MHC-II, and SIINFEKL-H-2Kb complex. Stained cells were analyzed by FCM.

### 3.5. Western blot analysis

THP-1 cells ($2 \times 10^6$ cells per well) were treated the following day with free OVA or OVA-loaded nanovaccine (20 μg/mL). After 24 h, cells were washed with PBS and lysed on ice using RIPA buffer. Protein lysates were centrifuged at 12000 rpm for 5 min at 4 °C, and the supernatants were collected for quantification using a BCA assay. Equal protein amounts were denatured at 100 °C for 10 min, separated by SDS-PAGE, and transferred onto polyvinylidene fluoride (PVDF) membranes. Membranes were probed with primary antibodies against STING, p-STING, p-TBK1, p-IRF3, and β-actin, followed by HRP-conjugated secondary antibodies. Bands were detected using ECL reagents and imaged with a chemiluminescence system.

### 3.6. ELISA detection

BMDCs and THP-1 cells were seeded into 24-well plates at a density of $1 \times 10^5$ cells per well and incubated with either free OVA or PEI-F-M + $Mn^{2+}$/OVA nanovaccine (20 μg/mL) for 4 h or 24 h. After incubation, the cell culture supernatants were collected and centrifuged to remove debris. The levels of IFN-β secretion in the supernatants were measured using IFN-β ELISA kit according to the manufacturer's instructions. Experiments were performed with three biological replicates ($n = 3$).

### 3.7. qPCR analysis

THP-1 cells were seeded into 24-well plates at a density of $1 \times 10^5$ cells per well and treated with either free OVA or PEI-F-M + $Mn^{2+}$/OVA nanovaccine (20 μg/mL) for 24 h. After treatment, total RNA was extracted using TRIzol or other RNA extraction reagents. The RNA was reverse-transcribed into cDNA using a reverse transcription kit. Subsequently, real-time quantitative PCR (qPCR) was performed using specific primers targeting IFN-β and CXCL10 genes. Three biological replicates ($n = 3$) were included. Relative mRNA expression levels were calculated by comparing Ct values.

### 3.8. In vivo activation and cross-presentation of DCs

Female C57BL/6 mice (6–8 weeks old) were randomly assigned into groups ($n = 4$ per group) and subcutaneously immunized on the right flank with PBS, free OVA (25 μg), or OVA-loaded nanovaccines (PEI-F/OVA, PEI-M + $Mn^{2+}$/OVA, PEI-F-M/OVA, PEI-F-M + $Mn^{2+}$/OVA, and PEI-F-M + free $Mn^{2+}$/OVA), each administered as 200 μL formulations containing 25 μg of OVA. After 72 h, mice were euthanized, and draining lymph nodes (dLNs) were collected and processed into single-cell suspensions by passing through a 200-mesh nylon cell strainer. Cells were first stained with Zombie Aqua™ viability dye to exclude dead cells, followed by surface staining with fluorophore-conjugated antibodies targeting CD11c, MHC-II, CD40, CD80, and the SIINFEKL-H-2Kb complex. Samples were analyzed by FCM to assess DCs activation and the extent of antigen cross-presentation.

### 3.9. Antigen-specific T cell response assays

Female C57BL/6 mice (6–8 weeks old) were randomly assigned to seven groups ($n = 4$ per group) and subcutaneously immunized on days 0 and 14 with either PBS, free OVA, or various OVA-loaded nanovaccine formulations (PEI-F/OVA, PEI-M + $Mn^{2+}$/OVA, PEI-F-M/OVA, PEI-F-M + $Mn^{2+}$/OVA, PEI-F-M + free $Mn^{2+}$/OVA). On day 21, splenocytes were harvested and re-stimulated in vitro with SIINFEKL peptide (10 μg/mL) or OVA protein (2 mg/mL) for 6 h, with a protein transport inhibitor added during the final 4 h to facilitate intracellular cytokine accumulation. Cells were stained with Zombie Aqua™ viability dye, followed by fluorophore-conjugated antibodies targeting CD3, CD8, IFN-γ, TNF-α, and IL-2, and analyzed by flow cytometry.

For enzyme-linked immunospot (ELISPOT) assays, $5 \times 10^5$ splenocytes per well were seeded into anti-IFN-γ pre-coated plates and stimulated with SIINFEKL peptide for 24 h. Cytokine-producing cells were quantified following the manufacturer's instructions.

### 3.10. B16-OVA melanoma tumor model

Female C57BL/6 mice (6–8 weeks old) were subcutaneously injected with $2 \times 10^5$ B16-OVA cells on the right dorsal flank. Mice were randomized into five groups ($n = 10$ per group) and vaccinated subcutaneously near the left inguinal lymph node with PBS, OVA, PEI-F/OVA, PEI-M + $Mn^{2+}$/OVA, or PEI-F-M + $Mn^{2+}$/OVA on days 3, 7, 11, and 15. Tumor size and body weight were recorded every other day. Tumor volume was calculated using the formula: 0.5 × length × width$^2$. Mice were euthanized when tumors reached 1500 $mm^3$.

On day 18, tumors, spleens, and lymph nodes were collected for flow cytometry analysis of $CD8^+$ T cells (granzyme B, IFN-γ, TNF-α), regulatory T cells (Tregs), myeloid-derived suppressor cells (MDSCs), and mature DCs. Splenic memory T cells were also analyzed. Tumor cytokines (IFN-γ, GZMB, IL-2) were quantified by ELISA. Safety was assessed by histology and serum biochemistry.

### 3.11. B16-OVA lung metastasis model

Female C57BL/6 mice (6–8 weeks old) were injected intravenously with $2 \times 10^5$ B16-OVA cells on day 0. Mice were randomized into four groups ($n = 4$ per group) and vaccinated subcutaneously near the right inguinal lymph node on days 3, 7, 11, and 15 with PBS, OVA, PEI-F/OVA, or PEI-F-M + $Mn^{2+}$/OVA. On day 25, lungs were harvested, imaged, and surface metastatic nodules were counted. Hematoxylin and eosin (H&E) staining was performed to assess the extent of pulmonary metastasis.

### 3.12. TC-1 tumor model

Female C57BL/6 mice (6–8 weeks old) were subcutaneously injected with $2.5 \times 10^5$ TC-1 cells on day 0. Mice were randomly divided into four groups ($n = 10$ per group) and vaccinated subcutaneously on days 3, 7, 11, and 14 with one of the following: PBS, free E7 peptide (GQAEPDRAMYNIVTFCCKCD), E7 peptide with CpG adjuvant (E7 + CpG), or PEI-F-M + $Mn^{2+}$/E7 nanovaccine, each administered as 200 μL formulations containing 5 μg E7 peptide. All formulations were freshly prepared.

On day 24, blood, tumors, spleens, and draining lymph nodes were harvested to analyze DC activation, T cell subpopulations, memory T cells, and cytotoxic $CD8^+$ T cell responses using flow cytometry. To assess immune memory, on day 56, tumor-free mice ($n = 5$ per group) along with naïve controls were rechallenged with $2.5 \times 10^5$ TC-1 cells

subcutaneously. Tumor growth was monitored thereafter. Frequencies of memory T cells and the expression of effector cytokines (IFN-γ, IL-2) were determined in spleens and lymph nodes.

### 3.13. Statistical analysis

All data were analyzed using GraphPad Prism software. Results are presented as mean ± standard deviation (s.d.). Statistical significance among multiple groups was determined via one-way ANOVA with Tukey's multiple comparisons test. Statistical significance among two groups was determined via two-tailed Student's *t*-test.

## 4. Conclusion

In this study, we developed a multifunctional nano-octopus vaccine based on the self-adjuvant polymer PEI-F-M coordinated with $Mn^{2+}$. This nanovaccine achieved efficient loading of the model antigen OVA, with an encapsulation efficiency exceeding 95.0%, through synergistic electrostatic interactions and metal coordination. Experimental results demonstrated that the nanovaccine not only significantly promoted DCs maturation but also enhanced type I interferon secretion via $Mn^{2+}$-mediated STING pathway. In the B16-OVA melanoma model, treatment with the nanovaccine resulted in remarkable antitumor efficacy, achieving 88.1% tumor growth inhibition and an 82.2% reduction in lung metastatic nodules. The nanovaccine induced robust antigen-specific $CD8^+$ T cells activation, while concurrently reducing the infiltration of immunosuppressive Tregs and MDSCs. Furthermore, in the TC-1 cervical cancer model, long-lasting memory T cells were detectable 60 days post-vaccination, and complete protection was observed upon secondary tumor challenge, confirming the vaccine's capacity to elicit durable immune memory. Overall, this work presents a streamlined nanovaccine strategy inspired by octopus tentacles and suckers, enabling high antigen loading, efficient cytosolic delivery, and immune activation. These features offer a promising solution to overcome key barriers in cancer vaccine development.

## CRediT authorship contribution statement

**Zijuan Wang:** Writing – review & editing, Writing – original draft, Data curation. **Yuanzhen Su:** Writing – review & editing, Writing – original draft, Data curation. **Shucheng Zhang:** Investigation. **Bingzheng Yu:** Formal analysis. **Dongbo Chen:** Supervision, Software. **Xiang Gao:** Methodology. **Yan Wei:** Formal analysis. **Irina A. Veselova:** Data curation. **Mingqiang Li:** Validation. **Shixian Lv:** Funding acquisition, Conceptualization.

## Ethics approval and consent to participate

All animals were purchased from Vital River Laboratory Animal Technology Co., Ltd. (Beijing, China). All animal experimentation protocols were approved by the Peking University Experimental Animal Center, with approval number MSE-LSX-2. This work reports no clinical trial or clinical samples.

## Declaration of competing interest

The authors declare that they have no known competing financial interests or personal relationships that could have appeared to influence the work reported in this paper.

## Acknowledgements

This work was supported by the National Key R&D Program of China (2025YFE0114200), the National Natural Science Foundation of China (No. 52273114, No. 82225012, No. 82430033, No. 32571686), Key Project of Science and Technology Plan of Beijing Education Commission (No. KZ20231002808), the Open Project Program of Yaoshan Laboratory (No. 2024001), the Key Science and Technology Project of Henan Province (No. 242300421207), Beijing Natural Science Foundation-Haidian Original Innovation Joint Fund Project (No. L222145), and the Beijing Municipal Science & Technology Commission (No. 221100007422088). The work was carried out under an agreement on the provision of grants from the federal budget in the form of subsidies in accordance with paragraph 4 of Article 78.1 of the Budget Code of the Russian Federation, dated August 20, 2025, No. 075-15-2025-639.

## Appendix A. Supplementary data

The data that support the findings of this study are available from the corresponding author upon reasonable request. Supplementary data to this article can be found online at https://doi.org/10.1016/j.jconrel.2025.114562.

## Data availability

Data will be made available on request.

## References

[1] M.J. Lin, J. Svensson-Arvelund, G.S. Lubitz, A. Marabelle, I. Melero, B.D. Brown, J. D. Brody, Cancer vaccines: the next immunotherapy frontier, Nat. Cancer 3 (8) (2022) 911–926.
[2] J. Liu, M.Y. Fu, M.N. Wang, D.D. Wan, Y.Q. Wei, X.W. Wei, Cancer vaccines as promising immuno-therapeutics: platforms and current progress, J. Hematol. Oncol. 15 (1) (2022) 28.
[3] W.T. Lei, K.X. Zhou, Y. Lei, Q. Li, H. Zhu, Cancer vaccines: platforms and current progress, Mol. Biomed. 6 (1) (2025) 3.
[4] B.J. Kim, N.S. Abdelfattah, A. Hostetler, D.J. Irvine, Progress in cancer vaccines enabled by nanotechnology, Nat. Nanotechnol. 20 (2025) 1–15.
[5] J.F. Yu, H. Sun, W.J. Cao, Y.P. Song, Z.X. Jiang, Research progress on dendritic cell vaccines in cancer immunotherapy, Exp. Hematol. Oncol. 11 (1) (2022) 3.
[6] M. Saxena, S.H. van der Burg, C.J.M. Melief, N. Bhardwaj, Therapeutic cancer vaccines, Nat. Rev. Cancer 21 (6) (2021) 360–378.
[7] Z. Hu, P.A. Ott, C.J. Wu, Towards personalized, tumour-specific, therapeutic vaccines for cancer, Nat. Rev. Immunol. 18 (3) (2018) 168–182.
[8] M. Kaczmarek, J. Poznanska, F. Fechner, N. Michalska, S. Paszkowska, A. Napierala, A. Mackiewicz, Cancer vaccine therapeutics: limitations and effectiveness-a literature review, Cells-Basel 12 (17) (2023) 2159.
[9] O.J. Finn, The dawn of vaccines for cancer prevention, Nat. Rev. Immunol. 18 (3) (2018) 183–194.
[10] S. Jhunjhunwala, C. Hammer, L. Delamarre, Antigen presentation in cancer: insights into tumour immunogenicity and immune evasion, Nat. Rev. Cancer 21 (5) (2021) 298–312.
[11] M. Durán-Lobato, A.M. López-Estévez, A.S. Cordeiro, T.G. Dacoba, J. Crecente-Campo, D. Torres, M.J. Alonso, Nanotechnologies for the delivery of biologicals: historical perspective and current landscape, Adv. Drug Deliver. Rev. 176 (2021) 113899.
[12] Y.Y. Ding, Y.X. Wang, Q.Y. Hu, Recent advances in overcoming barriers to cell-based delivery systems for cancer immunotherapy, Exploration 2 (3) (2022) 20210106.
[13] R.S. Riley, C.H. June, R. Langer, M.J. Mitchell, Delivery technologies for cancer immunotherapy, Nat. Rev. Drug Discov. 18 (3) (2019) 175–196.
[14] N. Pishesha, T.J. Harmand, H.L. Ploegh, A guide to antigen processing and presentation, Nat. Rev. Immunol. 22 (12) (2022) 751–764.
[15] S.M.G. Hayat, M. Darroudi, Nanovaccine: a novel approach in immunization, J. Cell. Physiol. 234 (8) (2019) 12530–12536.
[16] Y. Zhang, S.B. Lin, X.Y. Wang, G.Z. Zhu, Nanovaccines for cancer immunotherapy, WIREs Nanomed. Nanobiotechnol. 11 (5) (2019) e1559.
[17] M. Brisse, S.M. Vrba, N. Kirk, Y.Y. Liang, H. Ly, Emerging concepts and technologies in vaccine development, Front. Immunol. 11 (2020) 583077.
[18] S.Q. Huang, Y.N. Zhu, L. Zhang, Z.R. Zhang, Recent advances in delivery systems for genetic and other novel vaccines, Adv. Mater. 34 (46) (2022) 2107964.
[19] X.B. Zhang, B.W. Yang, Q.Q. Ni, X.Y. Chen, Materials engineering strategies for cancer vaccine adjuvant development, Chem. Soc. Rev. 52 (9) (2023) 2886–2910.
[20] L.Z. Mao, P.Q. Ma, X. Luo, H.W. Cheng, Z.X. Wang, E.Y. Ye, X.J. Loh, Y.L. Wu, Z. B. Li, Stimuli-responsive polymeric nanovaccines toward next-generation immunotherapy, ACS Nano 17 (11) (2023) 9826–9849.
[21] Y.F. Yi, M. Yu, W. Li, D.W. Zhu, L. Mei, M.T. Ou, Vaccine-like nanomedicine for cancer immunotherapy, J. Control. Release 355 (2023) 760–778.
[22] F. Danhier, E. Ansorena, J.M. Silva, R. Coco, A. Le Breton, V. Préat, PLGA-based nanoparticles: an overview of biomedical applications, J. Control. Release 161 (2) (2012) 505–522.

[23] D. Wibowo, S.H.T. Jorritsma, Z.J. Gonzaga, B. Evert, S.X. Chen, B.H.A. Rehm, Polymeric nanoparticle vaccines to combat emerging and pandemic threats, Biomaterials 268 (2021) 120597.
[24] D. Horvath, M. Basler, PLGA particles in immunotherapy, Pharmaceutics 15 (2) (2023) 615.
[25] M. Luo, H. Wang, Z.H. Wang, H.C. Cai, Z.G. Lu, Y. Li, M.J. Du, G. Huang, C. S. Wang, X. Chen, M.R. Porembka, J. Lea, A.E. Frankel, Y.X. Fu, Z.J.J. Chen, J. M. Gao, A STING-activating nanovaccine for cancer immunotherapy, Nat. Nanotechnol. 12 (7) (2017) 648–654.
[26] Z.T. Bennett, A. Krishnamurthy, S. Ye, V.S. Basava, Q. Feng, G. Huang, B.D. Sumer, J.M. Gao, A multi-threshold micelle improves tumor accumulation and STING immunotherapy, J. Am. Chem. Soc. 147 (23) (2025) 19547–19558.
[27] J.Y. Zhao, Y.D. Xu, S. Ma, Y.B. Wang, Z.C. Huang, H.Y. Qu, H.C. Yao, Y. Zhang, G. L. Wu, L.A. Huang, W.T. Song, Z.H. Tang, X.S. Chen, A minimalist binary vaccine carrier for personalized postoperative cancer vaccine therapy, Adv. Mater. 34 (10) (2022) 2109254.
[28] J. Xu, J. Lv, Q. Zhuang, Z.J. Yang, Z.Q. Cao, L.G. Xu, P. Pei, C.Y. Wang, H.F. Wu, Z. L. Dong, Y. Chao, C. Wang, K. Yang, R. Peng, Y.Y. Cheng, Z. Liu, A general strategy towards personalized nanovaccines based on fluoropolymers for post-surgical cancer immunotherapy, Nat. Nanotechnol. 15 (12) (2020) 1043–1052.
[29] Y. Chu, L.Y. Wang, X. Huang, C.X. Lao, L. Luo, J.Y. Chen, F.F. Jin, L.L. Zhao, K. Y. Hu, M. Lv, X.J. Li, Y. Yang, W.J. Zhao, W.G. Wang, Virus-mimicking nanoparticles potentiate in-situ cancer vaccines by reversing intratumoral DCs via stimulating cytosolic nucleic acid sensors, J. Control. Release 383 (2025) 113801.
[30] C.C. Feng, P. Tan, G.J. Nie, M.T. Zhu, Biomimetic and bioinspired nano-platforms for cancer vaccine development, Exploration 3 (3) (2023) 20210263.
[31] Y. Zhang, J. Chen, L. Shi, F. Ma, Polymeric nanoparticle-based nanovaccines for cancer immunotherapy, Mater. Horiz. 10 (2) (2023) 361–392.
[32] W. Jia, Y. Wu, Y. Xie, M. Yu, Y. Chen, Advanced polymeric nanoparticles for cancer immunotherapy: materials engineering, immunotherapeutic mechanism and clinical translation, Adv. Mater. 37 (8) (2025) e2413603.
[33] L.F. Ren, J. Lv, H. Wang, Y.Y. Cheng, A coordinative dendrimer achieves excellent efficiency in cytosolic protein and peptide delivery, Angew. Chem. Int. Ed. 59 (12) (2020) 4711–4719.
[34] L. Qin, H. Zhang, Y. Zhou, C.S. Umeshappa, H. Gao, Nanovaccine-based strategies to overcome challenges in the whole vaccination cascade for tumor immunotherapy, Small 17 (28) (2021) e2006000.
[35] G. Zhu, F. Zhang, Q. Ni, G. Niu, X. Chen, Efficient nanovaccine delivery in cancer immunotherapy, ACS Nano 11 (3) (2017) 2387–2392.
[36] X.L. Fang, H.R. Lan, K.T. Jin, D.J. Gong, J. Qian, Nanovaccines for cancer prevention and immunotherapy: an update review, Cancers 14 (16) (2022) 3842.
[37] H.Z. Ren, W.C. Jia, Y.J. Xie, M.H. Yu, Y. Chen, Adjuvant physiochemistry and advanced nanotechnology for vaccine development, Chem. Soc. Rev. 52 (15) (2023) 5172–5254.
[38] K.M. Garland, T.L. Sheehy, J.T. Wilson, Chemical and biomolecular strategies for STING pathway activation in cancer immunotherapy, Chem. Rev. 122 (6) (2022) 5977–6039.
[39] M.Z. Lv, M.X. Chen, R. Zhang, W. Zhang, C.G. Wang, Y. Zhang, X.M. Wei, Y. K. Guan, J.J. Liu, K.C. Feng, M. Jing, X.R. Wang, Y.C. Liu, Q. Mei, W.D. Han, Z. F. Jiang, Manganese is critical for antitumor immune responses via cGAS-STING and improves the efficacy of clinical immunotherapy, Cell Res. 30 (11) (2020) 966–979.
[40] K. Das, E. Belnoue, M. Rossi, T. Hofer, S. Danklmaier, T. Nolden, L.M. Schreiber, K. Angerer, J. Kimpel, S. Hoegler, B. Spiesschaert, L. Kenner, D. von Laer, K. Elbers, M. Derouazi, G. Wollmann, A modular self-adjuvanting cancer vaccine combined with an oncolytic vaccine induces potent antitumor immunity, Nat. Commun. 12 (1) (2021) 5195.
[41] J. Wang, S.X. Li, M.G. Wang, X. Wang, S.Q. Chen, Z.C. Sun, X.B. Ren, G. Huang, B. D. Sumer, N. Yan, Y.X. Fu, J.M. Gao, STING licensing of type I dendritic cells potentiates antitumor immunity, Sci. Immunol. 9 (92) (2024) eadj3945.